Subscriber access provided by UNIV TORONTO

Article

Metallic NiPS@NiOOH core-shell heterostructures as highly efficient and stable electrocatalyst for the oxygen evolution reaction

Bharathi Konkena, Justus Masa, Alexander J.R. Botz, Ilya Sinev, Wei Xia,
Jörg Kossmann, Ralf Drautz, Martin Muhler, and Wolfgang Schuhmann

ACS Catal., **Just Accepted Manuscript** • DOI: 10.1021/acscatal.6b02203 • Publication Date (Web): 18 Nov 2016

Downloaded from http://pubs.acs.org on November 19, 2016

Just Accepted

“Just Accepted” manuscripts have been peer-reviewed and accepted for publication. They are posted online prior to technical editing, formatting for publication and author proofing. The American Chemical Society provides “Just Accepted” as a free service to the research community to expedite the dissemination of scientific material as soon as possible after acceptance. “Just Accepted” manuscripts appear in full in PDF format accompanied by an HTML abstract. “Just Accepted” manuscripts have been fully peer reviewed, but should not be considered the official version of record. They are accessible to all readers and citable by the Digital Object Identifier (DOI®). “Just Accepted” is an optional service offered to authors. Therefore, the “Just Accepted” Web site may not include all articles that will be published in the journal. After a manuscript is technically edited and formatted, it will be removed from the “Just Accepted” Web site and published as an ASAP article. Note that technical editing may introduce minor changes to the manuscript text and/or graphics which could affect content, and all legal disclaimers and ethical guidelines that apply to the journal pertain. ACS cannot be held responsible for errors or consequences arising from the use of information contained in these “Just Accepted” manuscripts.

ACS Catalysis is published by the American Chemical Society. 1155 Sixteenth Street N.W., Washington, DC 20036

Published by American Chemical Society. Copyright © American Chemical Society. However, no copyright claim is made to original U.S. Government works, or works produced by employees of any Commonwealth realm Crown government in the course of their duties.

Metallic $NiPS_3$@NiOOH core-shell heterostructures as highly efficient and stable electrocatalyst for the oxygen evolution reaction

*Bharathi Konkena[†], Justus Masa[†], Alexander J. R. Botz[†], Ilya Sinev[‡], Wei Xia[‡], Jörg Koßmann[§], Ralf Drautz[§], Martin Muhler[‡], Wolfgang Schuhmann[†]**

[†] *Analytical Chemistry – Center for Electrochemical Sciences (CES); Ruhr-Universität Bochum, D-44780 Bochum (Germany); E-mail: wolgang.schuhmann@rub.de*

[‡] *Chair of Industrial Chemistry; Ruhr-Universität Bochum, D-44780 Bochum (Germany)*

[§] *Chair of Atomistic Modelling and Simulation, Ruhr-Universität Bochum, D-44780 Bochum (Germany)*

ABSTRACT: We report metallic $NiPS_3$@NiOOH core-shell heterostructures as an efficient and durable electrocatalyst for the oxygen evolution reaction exhibiting a low onset-potential of 1.48 V (vs RHE) and stable performance for over 160 h. The atomically thin $NiPS_3$ nanosheets are obtained by exfoliation of bulk $NiPS_3$ in the presence of an ionic surfactant. The OER mechanism was studied by a combination of SECM, *in-situ* Raman spectroscopy, SEM and XPS measurements, which enabled direct observation of the formation of a $NiPS_3$@NiOOH core-shell heterostructure at the electrode interface. Hence, the active form of the catalyst is represented as $NiPS_3$@NiOOH core-shell structure. Moreover, DFT calculations indicate an intrinsic metallic character of the $NiPS_3$ nanosheets with densities of states (DOS) similar to the bulk material. The high OER activity of the $NiPS_3$ nanosheets is attributed to a high density of accessible active metallic-edge and defect sites due to structural disorder, a unique $NiPS_3$@NiOOH core–shell heterostructure, where the presence of P and S modulates the surface electronic structure of Ni in $NiPS_3$, thus providing excellent conductive pathway for efficient electron-transport to the NiOOH shell. These findings suggest that good size control during liquid exfoliation may be advantageously used for the formation of electrically conductive $NiPS_3$@NiOOH core–shell electrode materials for the electrochemical water oxidation.

KEYWORDS: liquid exfoliation; metallic $NiPS_3$ nanosheets; oxygen evolution; $NiPS_3$@NiOOH core-shell heterostructure; electrocatalysis

1. INTRODUCTION

The design of efficient, affordable and cost effective electrocatalysts for water oxidation is of utmost necessity for viable hydrogen production through electrochemical water splitting.[1,2] The high energy demand of water electrolysers mostly accrues from the sluggish kinetics of the oxygen evolution reaction (OER), which remains frustratingly slow even for the most potent archetypical catalysts, RuO_2 and IrO_2, notwithstanding their scarcity and high cost.[3,4] Therefore, the necessity to develop robust low-cost catalysts for OER with high efficiency and stability cannot be overemphasized. Innumerable materials based on transition metal oxides,[5-8] phosphides,[9-11] sulphides[12-14] and two dimensional layered double hydroxides[15-17] have been considered as cost-effective alternatives to precious metal oxides. The field is rapidly expanding with nickel-, cobalt- and iron-based two dimensional layered materials and their composites being devoted as superior catalysts for OER. The main advantage of these 2D-layered sheets is the high aspect ratio in their dimensions facilitating the accessibility of exposed active “edge sites”, potentially enhancing their efficiency. Upon exfoliation, the electrocatalytic activity of the formed nanosheets correlates linearly with the number of edge sites, which in turn benefits from increased the edge exposure as the size decreases.[18-20] Exfoliation also creates more defective catalytic edge sites.[20] Owing to these facts, Ni-based catalysts with high electronic conductivity and a high density of accessible active sites would be more preferable to their semiconducting counterparts as potential candidates for advanced OER catalysts.[21,22]

Despite the recent outstanding performances towards electrocatalytic water oxidation reported for layered transition metal phosphides and sulphides,[9-14] systematic investigations on electrocatalytic water oxidation by transition metal chalcogenophosphates have to the best of our knowledge not yet been reported. The transition metal chalcogenophosphates, MPX_3, (M = Co, Mn, Fe, Ni and X = S, Se) are low cost and easily available layered materials with potential applications in electrochemistry.[23-25] For example, lithium intercalated nickel phosphorus trisulfide ($NiPS_3$) sheets have been exploited as efficient cathode materials for lithium ion batteries.[26,27] In $NiPS_3$, sulphide ions (S^{2-}) form a cubic close packed array with Ni atoms occupying 2/3rd of the octahedral vacancies with the remaining 1/3rd occupied by P-P pairs. Alternatively, the structure of the $NiPS_3$ compounds may be viewed as being built from MS_6 and P_2S_6 polyhedra that are linked by edge sharing to form sheets (Figure S1).[23] The $NiPS_3$ sheets stack one upon another to form 3D structures, the individual layers being held together by van der Waals interactions (Figure

1a).[28] For electrochemical applications, 2D structures are more desirable, thus making it necessary to devise simple routes for production of large quantities of 2D nano-sheets. Attention has mostly been focused on sonication-assisted exfoliation of 3D-sheets in a suitable solvent.[29] The resulting exfoliated sheets would, however, need to be stabilized by suitable surfactants to prevent restacking. The surfactant based exfoliation of inorganic layered materials including BN, MX_2 (M = Mo, W and X = S, Se), and transition metal oxides in aqueous media has been successfully used to produce single and few-layer nanosheets.[29]

Herein, we report a simple and highly effective means for liquid exfoliation of bulk $NiPS_3$ in the presence of an ionic surfactant yielding stable aqueous dispersions of ultra-thin $NiPS_3$ nanosheets. We demonstrate that the obtained nanosheets, covered with amorphous NiOOH, are highly efficient OER catalysts in alkaline media. Scanning electrochemical microscopy (SECM) *in-situ* electrochemistry-coupled Raman spectroscopy enabled direct observation of the surface reactions of the $NiPS_3$ nanosheets under OER conditions. Specifically, the formation of $NiPS_3$@NiOOH core-shell heterostructures is confirmed by SEM and XPS studies. DFT calculations indicate that the $NiPS_3$ nanosheets are intrinsically metallic, with densities of states (DOS) similar to the bulk material. The high OER activity of the catalyst is attributed to a high density of accessible active metallic-edge and defect sites due to structural disorder upon exfoliation as well as the unique $NiPS_3$@NiOOH core-shell heterostructure. The presence of P and S modulate the surface electronic structure of Ni, and the $NiPS_3$ core sustains high electronic conductivity due to its metallic nature.

2. EXPERIMAENTAL SECTION

2.1. Preparation of $NiPS_3$. $NiPS_3$ bulk crystals were prepared by the chemical vapor transport technique using excess sulphur as the transporting agent.[23,25] In a typical synthesis, elemental powders of nickel, phosphorus and sulphur were mixed in stoichiometric proportions and inserted into a quartz tube. The quartz tube was evacuated to ~10^{-6} mbar and sealed. The sealed quartz tube was placed in a tube furnace at 800°C for 2 weeks to ensure crystal formation. The quartz tube was cooled down to room temperature and opened to obtain the crystals.

2.2. Liquid exfoliation of bulk $NiPS_3$ crystals. Liquid exfoliation of bulk layered $NiPS_3$ crystals was achieved by dispersing 250 mg of the crystals in 50 mL of an aqueous solution containing CTAB (2mg/mL) as a surfactant, followed by sonication for 10 h in a 100 W bath sonicator. After sonication, the dispersions were subjected to differential centrifugation to narrow down the size distribution. In a typical procedure, the dispersions were centrifuged at 1000 rpm for 1 h, and the supernatant was separated and subjected to successive centrifugation at 3000 and 7000 rpm for periods of 2 h. The process is terminated at this stage (at 7000 rpm); the sediment is collected and re-dispersed in water under sonication. After sonication, a pink colored dispersion was obtained that was stable for at least 3 months without any flocculation and was used for further investigations.

2.3. Electrochemical methods. All electrochemical measurements were performed in a conventional three-electrode cell using an Autolab potentiostat/galvanostat (PGSTAT12, Metrohm-Autolab) coupled to a Metrohm RDE rotator. Disc-shaped glassy carbon of geometric area 0.126 cm^2 modified with the catalysts were used as the working electrode, a Ag/AgCl/3M KCl as the reference electrode and a platinum mesh as counter electrode. The measured potentials were converted to the reversible hydrogen electrode (RHE) scale using $E_{RHE} = E_{\mathrm{Ag/AgCl}} + 0.210\ \mathrm{V} + 0.059\ \mathrm{pH}$. Prior to the experiments, the glassy carbon electrode was polished on a polishing cloth using different alumina pastes (3.0 - 0.05 µm) to obtain a mirror-like surface, followed by ultrasonic cleaning in water. For electrochemical measurements a catalyst ink was prepared by dispersing 5.0 mg/mL of the catalyst in water and ultrasonicating for 30 min. 5.0 µL of the catalyst suspension was drop-coated onto the polished glassy carbon electrode and dried in air at room temperature. Before the OER measurements, modified electrodes were subjected to continuous potential cycling in the potential window of 0.1 V to 1.0 V vs RHE until reproducible voltammograms were obtained. Electrochemical impedance spectroscopy was performed in a frequency range from 50 kHz to 1 Hz at the corresponding open circuit potential of the electrode, using an AC perturbation of 10 mV$_{pp}$. The resistance of the solution was determined from the resulting Nyquist plot, and the latter was used for ohmic drop correction according to the relation, $E_c = E_m - iR_s$, where E_c is the corrected potential and E_m is the applied potential. All reported current densities were calculated using the geometric surface area of the electrode.

2.4. Electrodeposition of $Ni(OH)_2$. Thin films of nickel hydroxide with thicknesses of around a few equivalent monolayers were deposited on glassy carbon electrodes in aqueous 0.005 M $Ni(NO_3)_2$ solution by means of chronoamperometry at a potential of -1.0 V vs Ag/AgCl/3 M KCl for 150 s.[30] The electrodes were then thoroughly rinsed with water, dried at room temperature and further studied for OER.

2.5. In situ Raman spectroscopy. A specially designed Teflon cell was used employing graphite paper as working electrode. A platinum foil and Ag/AgCl/3M KCl served as counter electrode and reference electrode, respectively. $NiPS_3$ nanosheets were deposited on a gold coated silicon wafer and then placed on the graphite paper for collecting the Raman signals in KOH (pH 10) during potentiostatic polarization. Raman spectra were acquired using the Ar/Kr laser excitation of 661 nm with a Jobin-Yvon T64000 spectrometer equipped with a liquid nitrogen-cooled charge-coupled device (CCD) detector. A high numerical water-immersion optical 60x objective (laser spot 1 µm) was used for collecting the backscattered Raman signals. The incident laser power was 2-3 mW to avoid heating and degradation of the sample. The instrumental resolution was 2 cm^{-1} and acquisition time was 15 s.

2.6. DFT calculations. Density functional theory (DFT) calculations on the ideal bulk and two and single exemplary slabs were performed using the Vienna ab initio simulations package (VASP) code.[31,32] Perdew, Burke and Ernzernhof (PBE) exchange correlation functional approximation was used.[33] The Kohn-Sham one electron exchange wave functions were expanded by using a plane wave basis set with a kinetic energy cut-off of 400 eV. Using the Monkhorst-Pack scheme, the Brillouin zone was sampled with 10 × 10 × 10 (bulk) and 10 × 10 × 1 (slabs) k-points, respectively.[34] During geometry optimization, the atomic positions, lattice constants and unit cell shape of bulk were optimized until remaining forces lower than 0.01 eV/Å. The optimized bulk structure was then used to set up the slabs, for which the atomic positions were relaxed.

Afterwards, the total and projected densities of states were computed using 16 x 16 x 16 (bulk) and 16 x 16 x 2 (slabs) k-point meshes, respectively.

3. RESULTS AND DISCUSSIONS

Bulk $NiPS_3$ crystals were synthesized by means of the chemical vapor transport method[23,25] and further subjected to long-term ultra-sonication for 6 h to exfoliate the bulk crystals into ultra-thin sheets in the presence of the cationic surfactant, cetyltrimethylammonium bromide (CTAB).

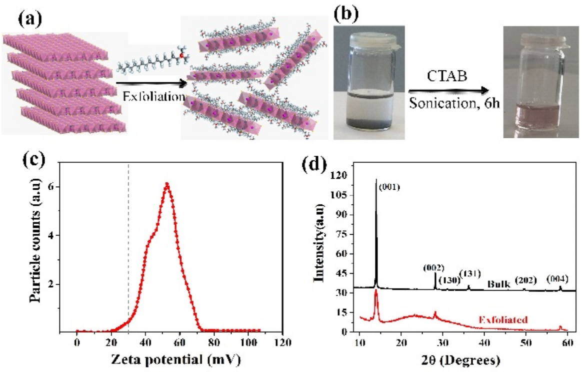

Figure 1. (a) Schematic illustration of liquid exfoliation of $NiPS_3$ bulk crystals. (b) Digital photographs of $NiPS_3$ dispersions before and after sonication. (c) Zeta potential distribution of the as-exfoliated CTAB-$NiPS_3$ aqueous dispersion. (d) XRD pattern of as prepared bulk and exfoliated $NiPS_3$ sheets.

After sonication, the dispersions were subjected to differential centrifugation speeds at 1000, 4000 and 7000 rpm successively, to narrow down the size distribution. The different sedimentation rates separate the differently sized nanosheets into a density gradient.[35] Excess of surfactant was removed by repeated washing with ethanol. The sediment was collected after 7000 rpm centrifugation, which forms a stable dispersion in water without any flocculation (Figure 1b). The stability of the colloidal dispersion was determined by zeta potential (ζ) measurements, which provide a measure of the magnitude and sign of the effective surface charge associated with the double layer around the colloidal particles. Generally, colloids with zeta potentials either greater than +30 mV or less than -30 mV are considered as stable dispersions.[36] The zeta potential distribution of CTAB-supported $NiPS_3$ nanosheets (Figure 1c), with the highest value of $\zeta \sim 52$ mV, indicates that the nanosheets have sufficient positive charge to form stable dispersions in water. These dispersions are stable for about 3 months clearly indicating that electrostatic repulsions between the positively charged $NiPS_3$ sheets are responsible for the stability of the dispersion. As there are no ionizable groups present on the sheets, the positive charge develops because of the interaction of the inorganic $NiPS_3$ sheet with the ionic surfactant. The CTAB surfactant chains are expected to be arranged randomly on the basal-plane of the $NiPS_3$ nanosheets (Figure 1b) with the charged head group exposed, as reported earlier for MoS_2 nanosheets.[37] Exfoliated $NiPS_3$ nanosheets were further characterized by XRD, XPS and Raman spectroscopy. Bulk $NiPS_3$ crystals showed an intense (*00l*) diffraction peak along with few weak (130), (131) and (202) peaks attributed to the cubic phase of $NiPS_3$ (Figure 1d) (JCPDS#01-078-0499). For the exfoliated nanosheets, all (*00l*) diffractions decreased in intensity with increasing fwhm, and the other reflections disappeared, suggesting a decrease in structural crystallinity, increase in disorder or defect density, and decrease in the particle size.

The bonding characteristics of the exfoliated $NiPS_3$ nanosheets were examined by X-ray photoelectron spectroscopy (XPS). A representative XPS spectrum for the Ni $2p_{3/2}$ core-level is shown in Figure 2a, which can be de-convoluted into four peaks. The main peak appears at 854.5 eV with three satellite features positioned at 855.5 eV, 859.6 eV and 864.3 eV. The presence of strong satellite features in the Ni 2p core level spectrum suggests an oxidation state of Ni^{II}. The S 2p core level spectrum consists of the spin-orbit split $2p_{3/2}$ and $2p_{1/2}$ peaks located at 162.2 eV and 163.4 eV, respectively (Figure 2b), indicating the exclusive presence of sulfide anions. Similarly, the P 2p core level spectrum has a spin-orbit split into the $2p_{3/2}$ and $2p_{1/2}$ peaks located at 132.5 eV and 133.4 eV, respectively (Figure 2c). Generally, the nature of the chemical bond can be derived from the separation between the binding energies of the core levels of the different atoms. For instance, the Ni $2p_{3/2}$ – S $2p_{3/2}$ separation is 692.3 eV in as-exfoliated $NiPS_3$ sheets, suggesting that Ni is octahedrally coordinated by S and the Ni-S bonds in $NiPS_3$ with ionic interactions formulated as $[Ni_2]^{4+}[P_2S_6]^{4-}$. These results are in good agreement with those previously reported for intercalated $NiPS_3$ sheets.[38-40] Furthermore, internal structural evidence, i.e. bonding vibrations of Ni^{2+} and $P_2S_6^{4-}$ ions were derived from the Raman spectra (Figure S2 and Table S4, see Supporting Information).

The surface morphology and the dimensionality of the exfoliated sheets were examined by AFM, SEM and TEM (Figure 3). The tapping mode AFM image (Figure 3a) and the corresponding height profile (Figure 3b) of the exfoliated $NiPS_3$ nanosheets reveal that the sheets are largely flat with an average thickness of 0.64 nm that corresponds to the thickness of a single $NiPS_3$ sheet amounting to 0.5 nm.[28] The lateral dimensions are typically ~500 nm, which is further confirmed by dynamic light scattering (DLS) measurements (Figure S3, see Supporting Information). The SEM image of bulk $NiPS_3$ crystals (Figure 3c) showed that the crystals are several micrometers (≥ 20 µm) in size, whereas for the exfoliated nanosheets (Figure 3d) the presence of two-dimensional ultra-thin sheets like morphology is clearly discernible, and the accessibility of exposed edge sites for the OER is certainly expected to be much higher in relation to the bulk $NiPS_3$. The presence of ripples and corrugations is found to be similar to other 2D nanostructures such as graphene and MoS_2.[29] TEM images of the exfoliated $NiPS_3$ sheets indicate two-dimensional ultrathin nanosheets with mean lateral dimensions ranging from 300 to 500 nm (Figure 3e). The indexed selected area electron diffraction pattern of individual layers (inset of Figure 3f) clearly reveals the cubic structure of $NiPS_3$ with space group C12/m1, consistent with XRD.[23] The in-layer structure of a single sheet was examined by high-resolution TEM. Figure 3f shows a typical single layer of $NiPS_3$ and lattice fringes with a *d*-spacing of 2.9 Å as expected for $NiPS_3$.[28] Further, EDS data confirm the expected presence of Ni, P and S elements with the respective stoichiometric compositions of $NiPS_3$ (Figure S4 and Figure S5, SI). It is worth noting that the ultra-sonication process retains the atomic structure of $NiPS_3$ without any appreciable change in chemical composition. For $NiPS_3$ nanosheets, the basal plane is flat at the atomic scale and can be considered as a nearly perfect single crystal due to the absence of unsaturated chemical bonds or free electrons.

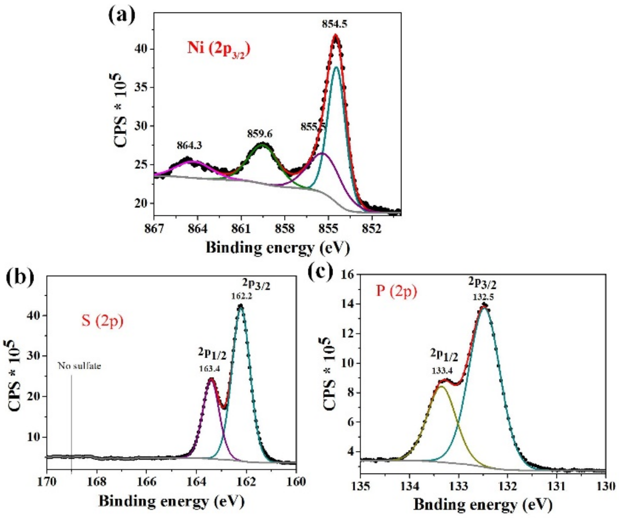

Figure 2. XPS spectra of the Ni $2p$, (b) S $2p$ and (c) P $2p$ core levels for the exfoliated $NiPS_3$ nanosheets. The binding energies of the peak positions are given in the figure. The C $1s$ peak binding energy (285 eV) was used as reference.

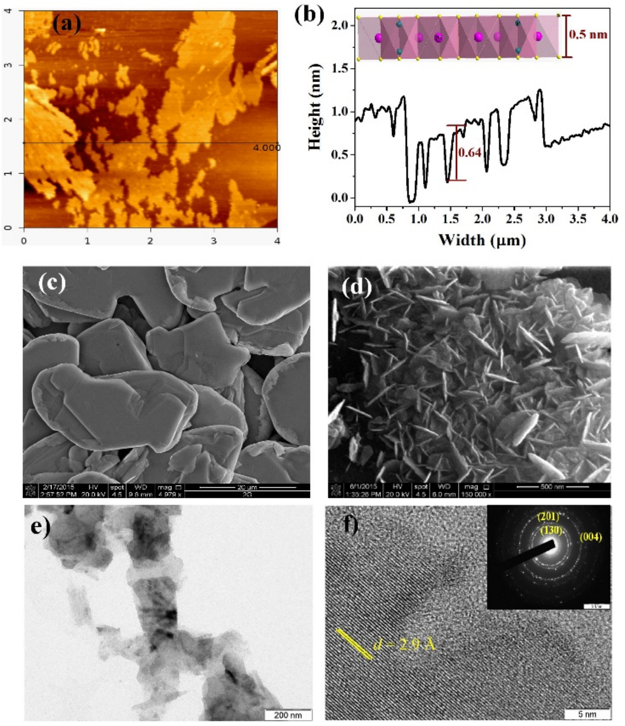

Figure 3. (a) Tapping mode AFM image of the exfoliated $NiPS_3$ nanosheets. (b) The height profile of the nanosheets as marked with the black line in Figure 3a. The inset in Figure 3b shows a structural model of a $NiPS_3$ sheet to indicate the thickness of a single layer. (c) SEM image of bulk $NiPS_3$ crystals. (d) SEM image of exfoliated $NiPS_3$ nanosheets. (e) TEM image of exfoliated $NiPS_3$ nanosheets. (f) HRTEM image of a single $NiPS_3$ layer. The inset shows the SAED pattern.

It is therefore unlikely that oxygen functional groups are chemically bound to its surface, except at highly strained defect sites.[41,42] The edge plane, however, is rough and with unsaturated valences. It is expected that most of the surface oxygen functional groups are attached on the edge planes. Edge sites have been previously shown to be the active sites in the Co- or Ni-promoted MoS_2 nanoclusters as hydro-desulfurization (HDS) catalysts.[43,44] Additionally, liquid exfoliation creates a high density of catalytic edge sites which are more exposed than the basal plane sites.[41] Therefore, whereas the active sites on the basal plane may also contribute to the OER, the edge and defect sites most evidently play a more pronounced role than in the case of the bulk material. The OER activity of $NiPS_3$ nanosheets was investigated in oxygen saturated 0.1 M KOH. Aqueous dispersions of the $NiPS_3$ nanosheets were deposited on a finely polished glassy carbon electrode, left to dry in air for 30 min and washed with ethanol to remove excess surfactant (Figure S6). Note that no binders were used. Prior to recording any OER activity data, the electrode was subjected to continuous polarization at a scan rate of 100 mV s^{-1} between 1.0 and 1.6 V until reproducible voltammograms were obtained. Results for the OER activity of the $NiPS_3$ nanosheets are shown in Figure 4a in the form of iR-corrected linear sweep voltammograms recorded at a scan rate of 5 mVs^{-1} and 1600 rpm of rotation to minimize the accumulation of gas bubbles on the electrode (For comparison, the LSV without iR-correction is provided as Figure S7; SI). For comparison, the catalytic activity of standard RuO_2, electrochemically deposited $Ni(OH)_2$ and bulk $NiPS_3$ were measured under similar loading and conditions.

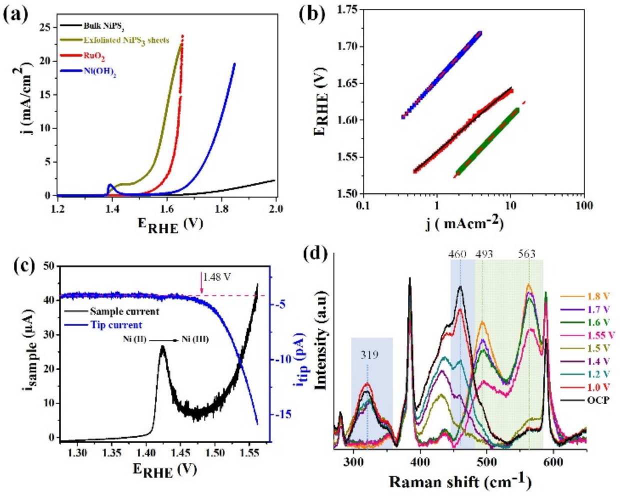

Figure 4. (a) Linear sweep voltammograms recorded at 1600 rpm and 5 mVs^{-1}. (b) Tafel plots are derived from data collected at a slow scan rate of 1 mVs^{-1}. (c) Oxygen evolution current measured at the SECM tip placed in close proximity to the $NiPS_3$ catalyst along with linear sweep voltammograms recorded at 1 mVs^{-1}. (d) *In-situ* Raman spectra of $NiPS_3$ nanosheets deposited on gold-coated silicon wafers recorded in KOH solution (pH~10) with an excitation wavelength of 661 nm. The Raman spectra were recorded at different working potentials vs RHE.

The bulk $NiPS_3$ crystals showed very poor OER activity in stark contrast to the exfoliated $NiPS_3$ nanosheets which exhibited extremely high activity. Notably, the $NiPS_3$ nanosheets attained a current density of 10 mA cm^{-2} (normalized to the geometric area of the electrode) at overpotential of 350 mV, which is significantly lower than that of the standard RuO_2 catalyst (410 mV) at the same current density. $Ni(OH)_2$ was even less active, requiring a more than 550 mV overpotential to generate a current density of 10 mA cm^{-2}. For the $NiPS_3$ nanosheets, the peak at 1.43 V is due to the oxidation of Ni^{II} to Ni^{III} leading to the formation of nickel oxyhydroxides NiOOH at the electrode surface,[45-47] revealing coverage on the surface of the $NiPS_3$ nanosheets with amorphous NiOOH. Tafel plots were extracted from slow scan voltammograms recorded at 1 mVs^{-1} to elaborate the mechanism and kinetics of the OER on the $NiPS_3$ nanosheets and

$$Ni(OH)_2 + OH- \xrightarrow{\qquad} NiO(OH) + H_2O + e^- \qquad (1)$$

on the electrodeposited $Ni(OH)_2$. In Figure 4b, the Tafel slope of Ni(OH)2 was 112 mV/dec, close to the theoretical value of (2.303RT)/αF), assuming a transfer coefficient (α) of 0.5.[48] This slope indicates that the first charge transfer step, in this case, the hydroxylation reaction (1), is rate determining. On the other hand, the Tafel slope for exfoliated $NiPS_3$ sheets was 80 mV/dec which suggests that a step involving both chemical and charge transfer reactions was rate-determining. Whereas the hydroxylation step on both $NiPS_3$ and $Ni(OH)_2$ (Figure 4a) appears to commence at the same potential (~1.4 V), the current rise is visibly steeper for electrodeposited $Ni(OH)_2$, indicative of a kinetically faster process. The onset potential for oxygen evolution on $Ni(OH)_2$, however, is much higher than on $NiPS_3$. This observation is consistent with Tafel analysis, and thus confirms that reaction (1) is indeed rate-limiting in the case of $NiPS_3$, while the subsequent steps are kinetically faster than on $Ni(OH)_2$.

Understanding the changes that occur on the electrode surface, especially, during OER including changes in the surface structure and composition is a key consideration in the development of efficient and stable catalysts for OER. Hence, scanning electrochemical microscopy (SECM) was employed to determine the onset potential of the OER and to *in-situ* probe interfacial electrochemical–chemical reactions during the OER (Supplementary Section 2).[49] In this experiment, a nanoelectrode (800 nm in diameter) was positioned at 4 μm from the surface of the electrocatalyst during OER and used as a sensor for detecting evolved oxygen. The cathodic current measured at the SECM tip along with the linear sweep voltammetry curves of OER for exfoliated nanosheets are shown in Figure 4c. The current at the tip increased sharply when the sample potential was 1.48 V, which corresponds to the onset potential for the OER. This value is 100 mV higher than the onset potential of 1.38V reported for Ni_3S_2 nanorods on nickel foam.[12] However, the onset potential of 1.48 V achieved for the $NiPS_3$ nanosheets is even lower than that reported recently by Stern et al. amounting to 1.5 V for a Ni_2P Janus type water splitting catalyst.[9] To the best of our knowledge, only a NiFe-double-layer hydroxide supported on carbon nanotubes was reported to attain a lower onset-potential of 1.47 V in 1 M KOH,[17] while a similar layered hydroxide in 0.1 M KOH afforded an onset-potential of 1.51 V.[45] Another well distinguished feature is the existence of the intense peak at 1.43 V which is due to the formation of $Ni^{III}O(OH)$ over the $NiPS_3$ electrode surface.[45,46] The Ni surface is spontaneously oxidized to $Ni^{II}(OH)_2$ upon immersion in 0.1 M KOH, and is converted to $Ni^{III}O(OH)$ before oxygen evolution can occur.[47] These features were not however clearly distinguishable from the RDE measurements (Figure S8). The formation of a $NiPS_3$@NiOOH core-shell heterostructure during oxygen evolution was probed in situ by electrochemistry coupled to Raman spectroscopy. Ni^{II} and Ni^{III} species were clearly identified by Raman spectroscopy acquired at different potentials beginning from the open-circuit potential and gradually increasing into the OER region. Potential-dependent vibrational features of Ni surface oxygen species are observed (Figure S9, SI). Attention is focused on the 250−650 cm^{-1} spectral range (Figure 4d), which is the fingerprint region for the different Ni oxidation states. At lower potentials, two broad features observed at 319 and 460 cm^{-1} can be assigned to the A_{1g} and E_{2g} lattice translational modes of $Ni\text{-}(OH)_2$.[50-53] As the potential is raised, the band at 460 cm^{-1} decreased in intensity and is completely absent at 1.5 V vs RHE. At 1.55 V, two new bands appear at 493 cm^{-1} and 563 cm^{-1}, assigned to lattice translational modes of Ni-OOH.[50,51] With further increase in potential, the ratio between the intensities is remaining constant, indicating no further transformation of NiO(OH). Notably, no appreciable change was noticed in the position of the vibrational bands of $Ni\text{-}PS_3$, P-P and S-S throughout the entire potential of $NiPS_3$ does not vanish during electrolysis (Figure S9; SI). Furthermore, XRD and XPS characterization of $NiPS_3$ nanosheets deposited on a glassy carbon plate before and after OER was performed in order to provide further insight about the structural composition of the catalyst during OER (Figure 5). After OER, the XRD pattern shows distinctive sharp peaks indexed to $NiPS_3$ and a broad feature at $2\theta = 25.1^\circ$ and 43° assigned to $Ni^{III}(OOH)$ consistent with the diffraction pattern reported for the γ-NiOOH phase (Figure 5a).[54]

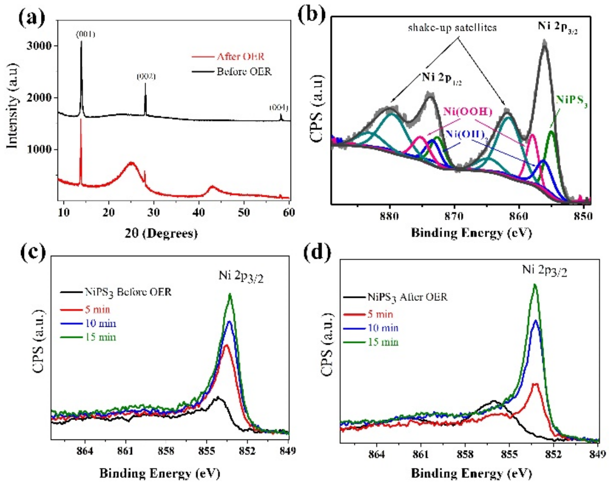

Figure 5. (a) XRD pattern of $NiPS_3$ nanosheets deposited on a glassy-carbon plate electrode recorded before and after the OER. (b) Ni *2p* core level XPS spectra recorded after OER. (c) High resolution depth-sputtering Ni *2p* core level XPS spectra recorded before OER, (d) after OER. Samples were sputtered with 2.5 keV Ar^+ ions in 5 min intervals. As the sputtering depth increases a stronger metallic Ni character is revealed.

A core/shell $NiPS_3$@NiOOH structure was identified by XPS analysis of the sample after OER testing (Figure 5b). The Ni 2p3/2 core level XPS spectrum clearly shows a higher degree of surface oxidation (coverage with oxygen species) compared to the sample before OER tests (Figure 2a and 5b). The Ni 2p peaks at 875.3 and 857.9 eV clearly represent Ni^{3+} oxidation state of NiOOH, whereas the peaks at 873.3 and 855.9 eV are attributed to a small amount of $Ni(OH)_2$. The Ni 2p peaks of

$NiPS_3$ is also observed after the OER (Figure 5b). XPS Ar^+ ion sputtering of the catalyst before and after OER provides additional evidence for the existence of a core/shell $NiPS_3$@NiOOH structure (Figure 5c and 5d). However, and most interestingly, after sputtering the surface with Ar^+ ions for only 5 min, the Ni 2 p3/2 core level XPS spectrum showed a lower degree of oxidation, a downward chemical shift of 2.9 eV from 856.1 eV to 853.2 eV, thus suggesting the existence of a very thin layer of NiOOH on the $NiPS_3$ sheets during OER (Figure 5c & 5d). As the sputtering depth increased, the characteristic features of $NiPS_3$ were restored. We also studied the surface elemental distribution of the catalyst using SEM (Figure S10) suggesting the coverage of NiOOH on the surface of $NiPS_3$. The stoichiometry of the constituent elements before and after OER was investigated using XPS (Figure S11 and S12; SI). Before OER, the electrode surface shows significant S and P surface enrichment. The atomic ratio of the elements change during the first 5 min of sputtering with Ar^+ ions, then stabilizes afterwards with further sputtering (Figure S12; SI). On the other hand, the atomic ratio of the elements for the sample after OER testing is invariable with sputtering time. On the basis of *in-situ* electrochemistry coupled to Raman spectroscopy data, XRD, SEM measurements and XPS post OER analysis, we can confidently conclude that a $NiPS_3$@NiOOH core-shell heterostructure exists at the electrode potentials applied for invoking the OER.

To gain some insight into the roles played by P and S in promoting the OER activity of $NiPS_3$, the performance of $NiPS_3$ was compared with NiS_2 and Ni_2P as similar Ni-based layered materials investigated under similar loading and conditions (Figure S13; SI). The $NiPS_3$ nanosheets showed significantly higher OER activity than NiS_2 and Ni_2P. The performances of Ni_2P and NiS_2 were, however, lower than reported in the literature, where the materials were supported on nickel foam.[9,10,12] The distinctive performance of $NiPS_3$ thus seems to arise from a synergistic effect between the P and S bonding with Ni. $NiPS_3$ consists of distorted $[P_2S_6]^{4-}$ clusters, and the P-S bond is more covalent in character than the P-P bond.[55] The actual mechanisms through which S and P enhance the OER performance are, however, still unclear. Obviously, the presence of P and S is expected to transform the surface electronic structure of nickel with ramifications on its electrocatalytic properties. The evidence for this can be inferred from the XPS analysis (SI data S8 and Table S5). The main binding energy (BE) of the 2 $p_{3/2}$ peak in $NiPS_3$ is at 854.5 eV, which is chemically shifted relative to that of pure elemental nickel expected at 852.6 eV. In addition, the surface electronic structure of Ni^{2+} in $NiPS_3$ is also different from that of Ni_2P and NiS/NiS_2 whose main 2 $p_{3/2}$ peaks occur at lower binding energies. The BE of elemental P in $NiPS_3$ positively shifts by about 2.5 eV in comparison to that of pure P (130. eV) and Ni_2P (129. 7 eV), indicating that P donates electrons to the more electronegative S ligand. Evidently, the electronegativity of the ligand (P and S) and the type of bonding orbitals of the dominant ligand, have a significant effect on the Ni 2 p main binding energies of these compounds. Moreover, after OER testing, the main $2p_{3/2}$ binding energy peak is centered at 856.1 eV, which is uniquely higher than the binding energy of the ordinary oxides and hydroxides of nickel which is expected at about 855.6 eV.

A combination of advanced in situ experiments and theoretical studies is necessary for a more elaborate elucidation of the OER mechanism and for unraveling the underlying factors responsible for the unique electrocatalytic behavior of $NiPS_3$ nanosheets. In this regard, theoretical investigations were implemented on exemplary bulk and monolayer of $NiPS_3$. According to the DFT calculations, bulk $NiPS_3$ shows a large local density of states (DOS) close to the Fermi level (Figure 6a), which reveals metallic behavior. The states close to the Fermi level arise from the delocalization of *d*-electrons of Ni and *p*-electrons of S atoms (Figure 6b, Figure S14). Interestingly, the DOS of single and two layer slabs are predicted to be very similar to the bulk (Figure 6a) implying that the thickness-independent electronic band structure of $NiPS_3$ cannot be expected to be the reason for its exceptional OER activity. The poor OER activity of bulk $NiPS_3$ in contrast to the nanosheets despite their similar electronic structure is therefore attributed to relatively lower exposure of catalytically active edge sites. Meanwhile, exfoliation confers the ultra-thin sheets a large specific surface area and a high density of defective active edge sites, as in the case of atomically thin $CoSe_2$ sheets.[42]

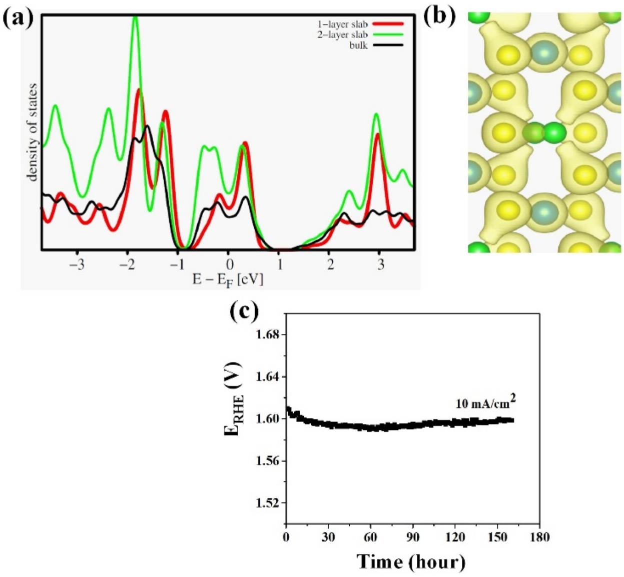

Figure 6. (a) Density of states of bulk, two and single slabs of $NiPS_3$. (b) Charge density iso-surface of the $NiPS_3$ nanosheet plotted at 0.1 eÅ^{-3}. (c) Galvanostatic durability test of the $NiPS_3$@NiOOH core-shell heterostructures at a current density of 10 mA cm^{-2}.

Ultrasonic treatment creates metal vacancies as defect sites, which are more favorable for adsorbing H_2O molecules.[42] Therefore, the high OER activity of the catalyst is attributed to the $NiPS_3$@NiOOH core-shell heterostructure formed at oxygen evolution conditions. For the ultrathin $NiPS_3$ nanosheets, the presence of P and S evidently modulates the electronic structure of Ni as revealed by XPS. The $NiPS_3$ core can contribute to enhancement of OER activity accruing from its metallic nature. Low electrical conductivity of nickel oxide and nickel hydroxide is one of the main drawbacks for their relatively lower OER activity compared to the outstanding activity exhibited by phosphorus and sulphur containing nickel catalysts.[9,12] Under OER conditions, the kinetics of oxygen evolution likely benefit from the unique NiOOH/$NiPS_3$ heterojunction band-structure, where the metallic core sustains relatively higher charge transfer kinetics compared to pure bulk nickel oxide or hydroxide. Consistent with this hypothesis, the $NiPS_3$ nanosheets act as a conducting support for in situ growth of highly active and stable Ni(OOH) nanosheets during OER. It is therefore the unique nature of the $NiPS_3$@NiOOH core-shell heterostructure, modification of the surface electronic structure of Ni by P and S, and the disorder in the structure of the $NiPS_3$ nanosheets that makes them exceptionally good OER catalysts compared to other Ni-based 2D-layered materials.

Finally, the stability of a given OER catalyst is a critical aspect for robust operation in any real application. $NiPS_3$ nanosheets were subjected to a stability test procedure involving acquisition of electrochemical impedance spectra (EIS), CV and galvanostatic electrolysis at 10 mA cm^{-2} for at least 160 h to assess the durability of the catalyst during oxygen evolution (Section S3, Figure S15; SI). Figure 6c shows the excellent stability of the exfoliated $NiPS_3$ catalyst during electrolysis at 10 mA cm^{-2} where a potential of 1.59 ± 0.02 is maintained during the 160 h of continuous operation. To determine the Faradaic efficiency, the liberated O_2 gas was quantitatively monitored by gas chromatography with a thermal conductivity detector (GC-TCD) during the first 5 h of the stability measurements. The O_2 produced during electrolysis using the $NiPS_3$@NiOOH core-shell structure was 1.71 mmol h^{-1} cm^{-2} (Figure S16; SI), with a Faradaic efficiency of 87 ± 3 %, confirming the high activity of the electrode material to efficiently catalyse the OER reaction in 0.1M KOH. Hence, our findings demonstrate the high potential of $NiPS_3$@NiOOH core-shell heterostructures as an efficient electrocatalyst for oxygen evolution electrodes.

4. CONCLUSIONS

In summary, ultra-thin $NiPS_3$ sheets are obtained by chemical exfoliation of bulk $NiPS_3$ in aqueous media in the presence of CTAB as ionic surfactant. The exfoliated sheets are typically less than 1 nm in thickness, indicating single layers stabilized by electrostatic repulsion between the positively charged sheets as a consequence of the adsorbed ionic surfactant. From SECM and *in-situ* Raman studies, Ni^{III} species (NiOOH) are identified over the $NiPS_3$ nanosheets as key intermediates during OER. Additionally, XRD XPS data and SEM analysis showed that $NiPS_3$ is not completely converted into NiOOH. A $NiPS_3$@NiOOH core-shell heterostructure is observed at the electrode surface during the electrolysis, which influences the mechanism and kinetics of the reaction. DFT calculations indicate a metallic character of the $NiPS_3$ nanosheets, and similar density of states as for bulk $NiPS_3$. The exceptionally high activity of the $NiPS_3$ nanosheets is ascribed to a high density of exposed active metallic-edge sites and the unique $NiPS_3$@NiOOH core-shell heterostructure, where the presence of P and S conducibly modifies the surface electronic state of nickel to enhance water oxidation. Under OER conditions, the metallic edge sites of the $NiPS_3$ core are expected to provide a favorable conducting pathway for efficient electron-transport to the NiOOH shell. The low cost and ease of exfoliation of metallic $NiPS_3$@NiOOH core-shell heterostructures with outstanding activity and stability makes them promising candidates for efficient water oxidation and possibly other applications in the field of catalysis.

ASSOCIATED CONTENT

Supporting Information. Supporting Information is available free of charge via the Internet at http://pubs.acs.org.
Structure of $NiPS_3$, size distribution of exfoliated $NiPS_3$, in-situ Raman spectroscopy, SEM/EDX images of the catalyst after OER, XPS analysis and computational figures and tables.

AUTHOR INFORMATION

Corresponding Author

* W. S.: E-mail, *wolfgang.schuhmann@rub.de*;
Tel, ++49 234 3226200; Fax, ++49 234 3214683

NOTES

The authors declare no competing financial interest.

ACKNOWLEDGMENT

The authors would like to thank Mrs. S. Schmidt and Mr. M. Trautmann for recording the SEM and AFM images. Financial support from the DFG (Deutsche Forschungsgemeinschaft) in the framework of the Cluster of Excellence RESOLV (EXC 1069) and the Ruhr-Universität Research Departments IFSC and MRD are gratefully acknowledged.

REFERENCES

(1) Kanan, M. W.; Nocera, D. G. *Science* **2008,** *32,* 1072–1075.

(2) Suntivich, J.; May, K. J.; Gasteiger, H. A.; Goodenough, J. B.; Shao-Horn, Y. *Science* **2011,** *334,*1383–1385.

(3) Walter, M. G.; Warren, E. L.; McKone, J. R.; Boettcher, S. W.; Mi, Q.; Santori, E. A.; Lewis, N. S. *Chem. Rev.* **2010,** *110*, 6446–6473.

(4) Lee, Y.; Suntivich, J.; May, K. J.; Perry, E. E.; Shao, H., Yang. *J. Phys. Chem. Lett.* **2012,** *3*, 399–404.

(5) McCrory, C. C. L.; Jung, S.; Peters, J. C.; Jaramillo, T. F. *J. Am. Chem. Soc.* **2013,** *135*, 16977–16987.

(6) Smith, R. D. L.; Prévot, M. S.; Fagan, R. D.; Trudel, S.; Berlinguette, C. P. *J. Am. Chem. Soc.* **2013,** *135*, 11580–11586.

(7) Masa, J.; Xia, W.; Sinev, I.; Zhao, A.; Sun, Z.; Grützke, S.; Weide, P.; Muhler, M.; Schuhmann, W. *Angew. Chem. Int. Ed.* **2014,** *53*, 8508–8512.

(8) Zhao, A.; Masa, J.; Xia, W.; Maljusch, A.; Willinger, M.-G.; Clavel, G.; Xie, K.; Schlögl, R.; Schuhmann, W.; Muhler, M. *J. Am. Chem. Soc.* **2014,** *136*, 7551–7554..

(9) Stern, L.-A.; Feng, L.; Song, F.; Hu, X. *Energy Environ. Sci.* **2015,** *8*, 2347–2351.

(10) Ledendecker, M.; Krick Calderón, S.; Papp, C.; Steinrück, H.-P.; Antonietti, M.; Shalom, M. *Angew. Chem. Int. Ed. [Online]* **2015**.

(11) Tian, J.; Liu, Q.; Asiri, A. M.; Sun, X. *J. Am. Chem. Soc.* **2014,** *136* (21), 7587–7590. DOI: 10.1021/ja503372r.

(12) Zhou, W.; Wu, X.-J.; Cao, X.; Huang, X.; Tan, C.; Tian, J.; Liu, H.; Wang, J.; Zhang, H. *Energy Environ. Sci.* **2013,** *6,* 2921.

(13) Peng, Z.; Jia, D.; Al-Enizi, A. M.; Elzatahry, A. A.; Zheng, G. *Adv. Energy Mater.* **2015,** *5*, 1402031–1402037.

(14) Kong, D.; Cha, J. J.; Wang, H.; Lee, H. R.; Cui, Y. *Energy Environ. Sci.* **2013,** *6*, 3553–3558.

(15) Song, F.; Hu, X. *Nature. Commun.* **2014,** *5*, 4477-1– 4477-9.

(16) Long, X.; Li, J.; Xiao, S.; Yan, K.; Wang, Z.; Chen, H.; Yang, S. *Angew. Chem. Int. Ed.* **2014,** *126*, 7714–7718.

(17) Gong, M.; Li, Y.; Wang, H.; Liang, Y.; Wu, J. Z.; Zhou, J.; Wang, J.; Regier, T.; Wei, F.; Dai, H. *J. Am. Chem. Soc.* **2013,** *135*, 8452–8455.

(18) Karunadasa, H. I.; Montalvo, E.; Sun, Y. J.; Majda, M.; Long, J.R.; Chang, C. J. *Science* **2012**, *335*, 698–702.

(19) Jaramillo, T. F.; Jorgensen, K. P.; Bonde, J.; Nielsen, J. H.; Horch, S.; Chorkendorff, I. Science **2007**, *317*, 100–102.

(20) Xie, J.; Zhang, H.; Li, S.; Wang, R.; Sun, X.; Zhou, M.; Zhou, J.; Lou, X. W.; Xie, Y. *Adv. Mater.* **2013**, *25*, 5807–5813.

(21) Xu, K.; Chen, P.; Li, X.; Tong, Y.; Ding, H.; Wu, X.; Chu, W.; Peng, Z.; Wu, C.; Xie, Y. *J. Am. Chem. Soc.* **2015,** *137* (12), 4119–4125.

(22) Ren, J.; Antonietti, M.; Fellinger, T. P. *Adv. Energy Mater.* **2015,** *5*, 1401660–1401665.

(23) Brec, R. *Solid State Ionics* **1986,** *22*, 3–30.

(24) Ouvrard, G.; Brec, R.; Rouxel, J. *Mat. Res. Bull.* **1985,** *20*, 1181–1189.

(25) N. Chandrasekharan; S. Vasudevan. *I. Phys.: Condens. Matter* **1994,** *6*, 4569–4579.

(26) Brec, R.; Schleich, D. M.; Ouvrard, G.; Louisy, A.; Rouxel, J. *Inorg. Chem.* **1979,** *18,* 1814 –1818.

(27) Kuzminskii, Y. V.; Voronin, B. M.; Redin, N. N. *J. Power Sources* **1995,** *55*, 133–141.

(28) Goossens, D. J.; James, D.; Dong, J.; Whitfield, R. E.; Norén, L.; Withers, R. L. *J. Phys. Condens Matter* **2011,** *23*, 65401-1–65401-7.

(29) Nicolosi, V.; Chhowalla, M.; Kanatzidis, M. G.; Strano, M. S.; Coleman, J. N. *Science* **2013**, *340*, 1226419-1–1226419-18.

(30) Zhao, D. D.; Bao, S. J.; Zhou, W. J.; Li, H. L. *Electrochem. Commun.* **2007,** *9*, 869–874.

(31) Kresse, G.; Furthmüller, J. *Comput. Mater. Sci.* **1996,** *6*, 15–50.

(32) Kresse, G.; Furthmüller, J. *Phys. Rev. B* **1996,** *54*, 11169–11186.

(33) Perdew, J. P.; Burke, K.; Ernzerhof, M. *Phys. Rev. Lett.* **1996,** *77*, 3865–3868.

(34) Monkhorst, H. J.; Pack, J. D. *Phys. Rev. B* **1976,** *13*, 5188–5192.

(35) Konkena, B.; Vasudevan, S. *J. Phys. Chem. C* **2014,** *118*, 21706–21713.

(36) Konkena, B.; Vasudevan, S. *J. Phys. Chem. Lett.* **2012,** *3*, 867–872.

(37) Gupta, A.; Arunachalam, V.; Vasudevan, S. *J. Phys. Chem. Lett.* **2015,** *6*, 739–744.

(38) Curro, G. M. Grasso, V. Neri, F. Silipigni, L. *Il Nuovo Cimento* **1995,** *17D*, 38–52.

(39) Manova, E.; Severac, C.; Andreev, A.; Clément, R. *J. Catal.* **1997,** *169*, 503–509.

(40) Piacentini, M. Khumalo, F. S. Olson, C. G. Anderegg, J. W. Lynch, D. W. *Chem. Phys.* **1982,** *65*, 289–304.

(41) Voiry, D.; Yamaguchi, H.; Li, J.; Silva, R.; Alves, D. C. B.; Fujita, T.; Chen, M.; Asefa, T.; Shenoy, V. B.; Eda, G.; Chhowalla, M. *Nature. Mater.* **2013,** *12*, 850–855.

(42) Liu, Y.; Cheng, H.; Lyu, M.; Fan, S.; Liu, Q.; Zhang, W.; Zhi, Y.; Wang, C.; Xiao, C.; Wei, S.; Ye, B.; Xie, Y. *J. Am. Chem. Soc.* **2014,** *136*, 15670–15675.

(43) Yoosuk, B.; Kim, J. H.; Song, C.; Ngamcharussrivichai, C.; Prasassarakich, P. *Catal. Today* **2008,** *130*, 14–23.

(44) Lauritsen, J. V.; Kibsgaard, J.; Helveg, S.; Topsøe, H.; Clausen, B. S.; Laegsgaard, E.; Besenbacher, F. *Nature Nanotech.* **2007,** *2* (1), 53–58. DOI: 10.1038/nnano.2006.171.

(45) Louie, M. W.; Bell, A. T. *J. Am. Chem. Soc.* **2013,** *135*, 12329–12337.

(46) Lu, X.; Zhao, C. *Nature. Commun.* **2015,** *6*, 6616-1– 6616-7.

(47) Trotochaud, L.; Young, S. L.; Ranney, J. K.; Boettcher, S. W. *J. Am. Chem. Soc.* **2014,** *136*, 6744–6753.

(48) Bockris, J. O.; Otagawa, T. *J. Phys. Chem.* **1983,** *87*, 2960–2971.

(49) Botz, A. J.; Nebel, M.; Rincón, R. A.; Ventosa, E.; Schuhmann, W. *Electrochim. Acta* **2015**, *179*, 38-44.

(50) Bantignies, J. L.; Deabate, S.; Righi, A.; Rols, S.; Hermet, P.; Sauvajol, J. L.; Henn, F. *J. Phys. Chem. C* **2008,** *112* , 2193–2201.

(51) Deabate, S.; Fourgeot, F.; Henn, F. *J. Power Sources* **2000,** *87*, 125–136.

(52) Desilvestro, J.; Corrigan, D. A.; Weaver, M. J. *J. Phys. Chem.* **1986,** *90*, 6408–6411.

(53) Yeo, B. S.; Bell, A. T. *J. Phys. Chem. C* **2012,** *116*, 8394–8400.

(54) Barnard, R.; Crickmore, G. T.; Lee, J. A.; F. L. Tye. *J. Appl. Electrochem* **1980,** *10*, 61–70.

(55) Ohno, Y. *J. Solid State Chem.* **1986,** *63*, 258–266.

Metallic $NiPS_3$@NiOOH core-shell heterostructures as highly efficient and stable electrocatalyst for the oxygen evolution reaction

Bharathi Konkena[†], *Justus Masa*[†], *Alexander J. R. Botz*[†], *Ilya Sinev*[‡], *Wei Xia*[‡], *Jörg Koßmann*[§], *Ralf Drautz*[§], *Martin Muhler*[‡], *Wolfgang Schuhmann*[†]*

SYNOPSIS TOC

We exploited a unique combination of S and P in a single material as a $NiPS_3$ to develop an exceptionally active and stable electro catalyst for water oxidation. The high OER activity of the catalyst nanosheets is attributed to a high density of accessible active site, including edge and defect sites, due to structural disorder, and a unique $NiPS_3$@NiOOH core-shell heterostructure, where the presence of P and S modulate the surface electronic structure of NiOOH, while the core ($NiPS_3$) provides a conductive pathway for efficient electron-transport to the NiOOH shell.